PAPER

Check for updates

Solvation effect on the ESIPT mechanism of nitrile-substituted *ortho*-hydroxy-2-phenyl-oxazolines

Hengwei Zhang,[a] Wenzhi Li,[a] Yuxi Wang,[a] Yaping Tao,[b] Yi Wang, [ID][a] Fan Yang*[a] and Ziqing Gao [ID] *[a]

In this study, density functional theory (DFT) and time-dependent density functional theory (TD-DFT) were used to unveil the solvation effects on the excited-state intramolecular proton transfer (ESIPT) of nitrile-substituted *ortho*-hydroxy-2-phenyl-oxazoline (NOHPO) molecules in three different solvents. According to the functional analysis of the reduced density gradient, hydrogen bond in low-polar solvents is stronger compared to that in high-polar solvents, indicating that proton transfer (PT) can be influenced by the polarity of the solvent. Moreover, the geometric parameters and infrared vibration spectrum of NOHPO in different types of solvents in the S_0 and S_1 state were compared, which confirmed the above results. By analyzing electronic spectra and frontier molecular orbitals, it was found that the spectral properties were affected by different polar solvents. Molecular electrostatic potential surface calculations proved that PT took place between the H_2 atom and N_3 atom, and the natural population analysis and Hirshfeld charge reveal the charge distribution after photoexcitation. To investigate the ESIPT progress intensively, the potential energy curves of NOHPO in three types of solvents were established. The findings revealed that NOHPO could transform from enol to keto form in the S_1 state spontaneously, and ESIPT progress was promoted with the decrease in polarity.

Introduction

Excited-state intramolecular proton transfer (ESIPT), one of the most elementary processes in chemistry and biology, plays a crucial role in photophysics, photochemistry, and photobiology.[3–6] Since Weller *et al.* observed a large Stokes shift in salicylic acid and found the reaction of ESIPT, ESIPT has received considerable attention from experimental and theoretical chemists.

The ESIPT progress needs proper distance between the proton donor and proton acceptor to form intramolecular hydrogen bonds, so that the ESIPT reaction may occur after photoexcitation. The hydrogen bond is an important part of ESIPT; consequently, the theory of hydrogen bond enhancement in the excited state has been proposed and has proven numerous mechanisms of ESIPT.[7–20] ESIPT is very common in organisms, whether it is a vision circle or the luminescence of green fluorescent protein, they are all relevant to it.[21–23] Apart from natural ESIPT progress, an ESIPT unit can be synthesized chemically to mimic the optical performance of green fluorescent protein; we can even get excellent fluorescent materials with high fluorescence efficiency and narrow bandwidth.[24] The most important application of ESIPT is the chemical sensor, which is designed by the ESIPT mechanism

and is highly selective and highly efficient in detecting inorganic ions, such as Zn^{2+},[25] Cu^{2+},[26] Al^{3+},[27] and As^{3+}.[28] Due to the characteristics of ESIPT, some researchers have reported on dual-channel chemical sensors based on ESIPT for detecting Al^{3+}/F^-,[29] Zn^{2+}/Cd^{2+},[30] Cu^{2+}/Fe^{3+},[31] *etc.* In addition to detecting inorganic compounds, an ESIPT sensor can also detect organic compounds, and it has been widely used *in vivo* detection. Compared to other traditional methods (HPLC or MS), fluorometric detection has great selectivity, sensitivity, and *in vivo* imaging capability. Among them, chemical sensors based on ESIPT have been a widespread concern due to their ultra-fast reaction rate and large Stokes shift, which impede auto-fluorescence in imaging.[32,33]

Although ESIPT is widely used in chemical sensors, the application of ESIPT also faces numerous challenges. For example, the ESIPT unit may happen concurrently with non-radiative quenching processes, resulting in low emission efficiency and quantum yields. In addition, the oversized ESIPT molecule could influence metabolite traffic within cells in bio-imaging.[34] Therefore, it is meaningful to design an organic molecule with minimalistic and bright fluorescence for bio-imaging and fluorescent sensors. Nitrile-substituted *ortho*-hydroxy-2-phenyl-oxazolines (NOHPOs) with extremely efficient, low molecular weight, single-benzene fluorophores, have been synthesized in the experiment.[35] In the experiment, NOHPOs in different solvents have been studied, but the solvation effect on the ESIPT progress has not been discussed in detail. Therefore, the influence of the different solvent on the ESIPT progress of

[a]*School of Biological Engineering, Dalian Polytechnic University, Dalian 116034, P. R. China. E-mail: wangyi@dlpu.edu.cn; gao_zq@dlpu.edu.cn; Fax: +86 0411 86323646; Tel: +86 0411 86323646*

[b]*College of Physics and Electronic Information, Luoyang Normal University, Luoyang 471022, P. R. China*

NOHPO should be investigated to grasp its ESIPT mechanism and develop more efficient ESIPT units.

In the present study, we will theoretically reveal the ESIPT progress of NOHPO in three different solvents: acetonitrile (ACN), dichloromethane (DCM), and cyclohexane (CH). We use DFT and TD-DFT in the S_0 and S_1 states to optimize all configurations. To compare the hydrogen bond strength in ACN, DCM, and CH by analyzing the infrared vibrational spectra (IR), the functional analysis of reduced density gradient (RDG) isosurfaces and scatter plots was carried out. The frontier molecular orbitals (FMOs), molecular electrostatic potential surface (MEPS), natural population analysis (NPA), and Hirshfeld charge are analyzed to research the charge distribution. More importantly, we established potential-energy curves (PECs) to further illustrate the mechanisms of ESIPT.

Computational methods

The Gaussian 16 program[36] was used to perform all of the theoretical calculations reported in this study. We used DFT and TD-DFT methods with B3LYP-D3(BJ)[37–42] functional and TZVP[43,44] basis sets to calculate the geometric optimizations in the ground (S_0) and first singlet excited state (S_1). To ensure the optimized structures at minima without imaginary frequency, we also analyzed vibration frequencies. The polarizable continuum model (PCM) with the integral equation formalism variant (IEF-PCM) was used in our calculations. IEF-PCM was used in three types of solvents (ACN: $\varepsilon = 35.688$, DCM: $\varepsilon = 8.93$, CH: $\varepsilon = 2.0165$). The potential energy curves (PECs) were scanned in the S_0 and S_1 states to further investigate the ESIPT process, and the N–H bond length (0.05 Å) decreased with a constant step in the S_0 state and the O–H bond length (0.05 Å) was decreased with a constant step in the S_1 state.

The hydrogen bond strength in numerous solvents was compared using the RDG function,[45] and the results were calculated and plotted using the Multiwfn software[46] and VMD program.[47]

Result and discussion

Geometric structures, IR vibrational spectra, RDG isosurfaces

The geometric structures of NOHPO molecules were optimized at the B3LYP-D3(BJ)/TZVP level in the S_0 and S_1 states, as shown in Fig. 1.
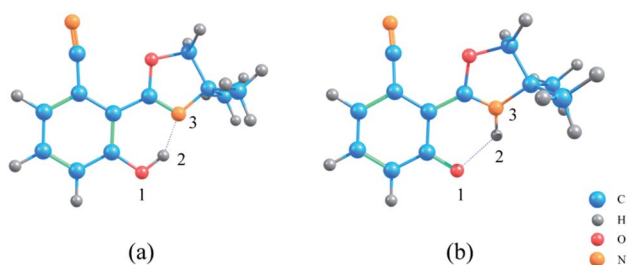

Fig. 1 The optimized structures of NOHPO molecules: (a) S_0 state and (b) S_1 state.

Table 1 The calculated primary bond lengths (Å) and angels (°) in the S_0 and S_1 states for NOHPO in different types of solvents

	ACN		DCM		CH	
	S_0	S_1	S_0	S_1	S_0	S_1
O_1–H_2	1.007	1.963	1.006	1.958	1.003	1.940
H_2–N_3	1.646	1.018	1.650	1.019	1.661	1.021
$\delta(O_1$–H_2–$N_3)$	147.869	125.451	147.767	125.713	147.413	126.464

Table 1 shows the primary bond lengths and angles. The hydrogen bond of H_2–N_3 turns to covalent bond in the S_1 state, and its bond length decreases in the trend 0.628 Å (ACN) < 0.631 Å (DCM) < 0.640 Å (CH) in three types of solvents, respectively. Therefore, the hydrogen bond is enhanced in the S_1 state. The bond length of O_1–H_2 in ACN, DCM, and CH are extended from 1.007, 1.006 and 1.003 Å to 1.963, 1.958 and 1.940 Å, respectively. This phenomenon shows that in the S_1 state, O_1–H_2 binding is weakened.

The IR vibration frequency analysis is a good way to analyze the strength of the hydrogen bond. In order to test the hydrogen bond strength, H_2–N_3 is analyzed in three types of solvents. Fig. 2 shows frequencies in ACN, DCM, and CH are 3476 cm^{-1}, 3466 cm^{-1}, 3432 cm^{-1}, respectively, which indicates that the ESIPT reaction occurs more easily in low-polar solvents.

In addition, the RDG function is used to distinguish different weak interactions mainly to unveil the characters of the hydrogen bonds.[1,2] As shown in Fig. 3, the scatter graphs show the weak interactions and the strength of the hydrogen bond in numerous solvents. In Fig. 3(a), blue represents the hydrogen bond, green represents van der Waals interactions and red represents nonbond repulsive interaction. The bluer the isosurfaces, the stronger the hydrogen bond strength is. By comparing the color of RDG isosurfaces in Fig. 3, the hydrogen bond strength in CH is the strongest. Fig. 3(b) shows the hydrogen bond strength in the S_1 state in three types of solvents. With the increase in the absolute value of sign((λ2) ρ(r)), the strength of the hydrogen bond is enhanced. As the result, the hydrogen bond strength in three types of solvents orders by CH
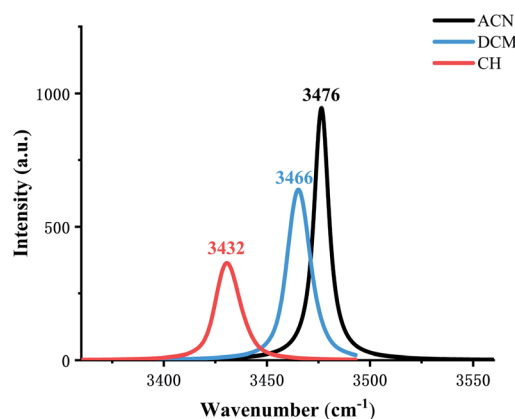

Fig. 2 Calculated stretching vibrational frequencies of the H_2–N_3 bond in the S_1 state in three types of solvents.
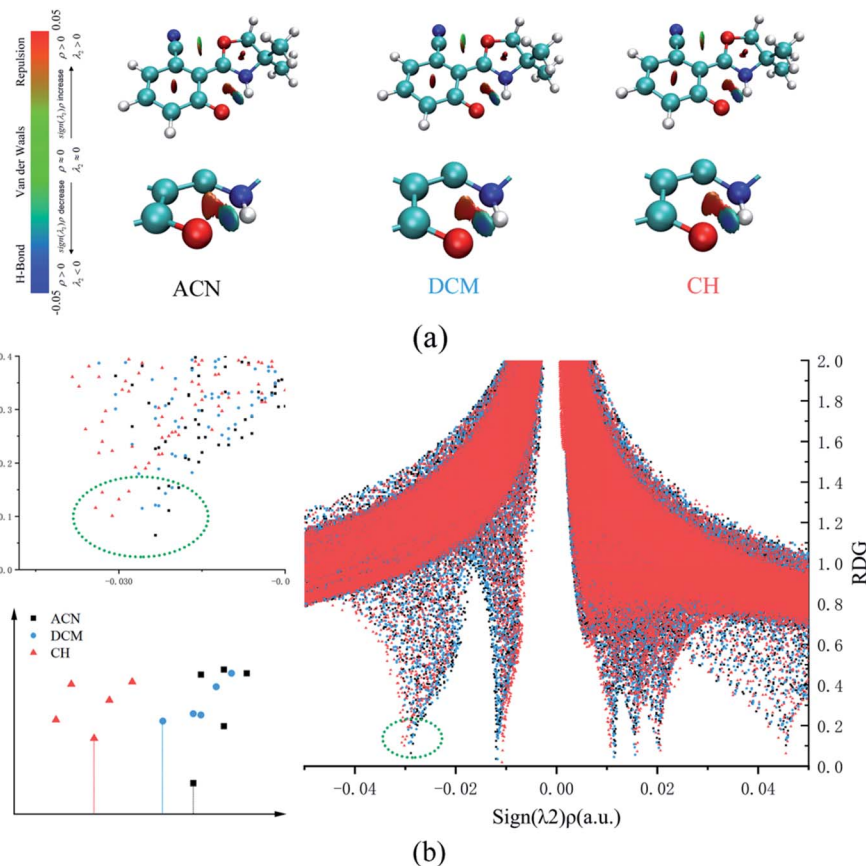
Fig. 3 (a) The visual diagram of RDG isosurfaces and the color gradient axis. (b) Scatter graphs of the reduced density gradient (RDG(r)) versus $\Omega(r)$ in three types of solvents.

> DCM > ACN. The above result can also prove that the intensity of the hydrogen bonds is reinforced as the polarity decreasing.

Electronic spectra, FMOs, MEPS, charge distribution

Fig. 4 shows the calculated absorption and fluorescence spectra in three different solvents. The calculated absorption peaks (ACN: 315 nm, DCM: 313 nm, CH: 309 nm) and fluorescence emission peaks (ACN: 468 nm, DCM: 470 nm, CH: 482 nm) are in accord with

the experimental data.[35] The Stokes shift in three different solvents is 153 nm, 157 nm, and 173 nm, respectively. The calculated results show that emission is completely from keto tautomer. Furthermore, with the decrease in the polarity of the solvent, the maximum emission wavelength (from 468 nm to 482 nm) of the fluorescence spectrum exhibits a bathochromic shift and the Stokes shift enlarged. The influence of the solvent environment on the electronic configuration could cause different solvent chromic effects.
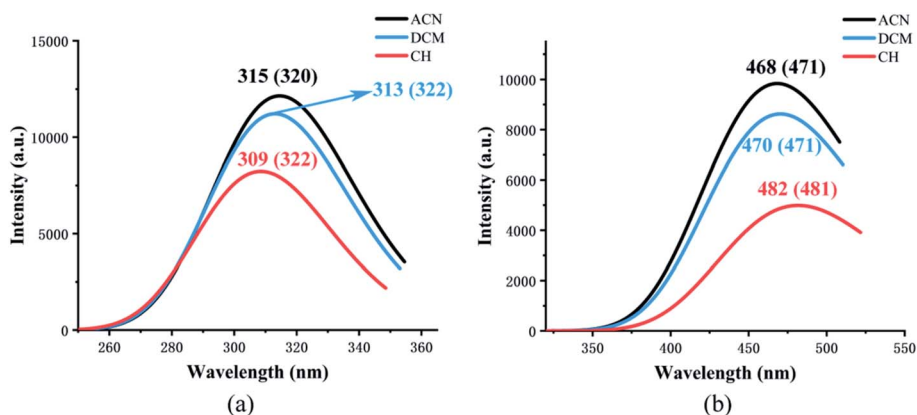

Fig. 4 The calculated absorption (a) and fluorescence (b) wavelength of NOHPO in different kinds of solvents. The values in parentheses are experimental data.[35]

Table 2 The electronic excitation energy (nm), corresponding oscillator strength (f) of the low-lying electronically excited states for NOHPO in three types of solvents, as well as orbital transition (OT) contributions to the electronic excited states (CI)

		Transition	λ (nm eV^{-1})	f	OT	CI (%)
ACN	Absorption	$S_0 \rightarrow S_1$	315/3.93	0.3005	H $\rightarrow$ L	96.5%
	Emission	$S_1 \rightarrow S_0$	468/2.65	0.2433	L $\rightarrow$ H	96.9%
		$S_2 \rightarrow S_0$	389/3.18	0.0333	L $\rightarrow$ H−1	95.7%
DCM	Absorption	$S_0 \rightarrow S_1$	313/3.96	0.2777	H $\rightarrow$ L	96.1%
	Emission	$S_1 \rightarrow S_0$	470/2.64	0.2133	L $\rightarrow$ H	95.6%
		$S_2 \rightarrow S_0$	394/3.15	0.0393	L $\rightarrow$ H−1	94.4%
CH	Absorption	$S_0 \rightarrow S_1$	309/4.02	0.2036	H $\rightarrow$ L	94.7%
	Emission	$S_1 \rightarrow S_0$	482/2.57	0.1234	L $\rightarrow$ H	88.4%
					L $\rightarrow$ H−1	11.1%
		$S_2 \rightarrow S_0$	408/3.04	0.0554	L $\rightarrow$ H−1	87.2%
					L $\rightarrow$ H	11.3%

As is known, charge could be transferred and redistributed after photoexcitation. The molecular charge analysis provides proper evidence for the determination of what drives the proton transfer process. FMOs are studied in order to gain a better understanding of the ESIPT reaction. The results are listed in Table 2. The oscillator strength of NOHPO in the S_1 state is 0.3005 (ACN), 0.2777 (DCM), and 0.2036 (CH). Fig. 5 shows the FMOs of NOHPO and the energies in the highest occupied molecular orbital (HOMO) and the lowest unoccupied molecular orbital (LUMO) in ACN, DCM and CH. In the S_1 state, the orbital transition only happens from HOMO to LUMO. Hence, only HOMO and LUMO are shown in Fig. 5. The HOMO displays π characteristic and the LUMO displays π^* characteristic, so the orbital composition from HOMO to LUMO (96.5% for ACN, 96.1% for DCM, and 94.7% for CH) could be assigned the dominant $\pi\pi^*$-type transition. Hence, the systems from S_1 to S_0 are more likely to get deactivated by radiation (emitting fluorescence), rather than by non-radiation. It is clear that the transition energies in ACN, DCM and CH are different, which

indicates that the polarity of the solvents can affect the ESIPT progress of NOHPO.

MEPS (molecular electrostatic potential surface) has been widely used to investigate the electrostatic interaction, predicting the reaction sites and properties of the molecule, particularly in the study of intramolecular or intermolecular hydrogen bonding interactions. Fig. 6 shows NOHPO molecules in the S_0 state in the ACN solvent. It is clear that there is a drastic polarization distribution of negative and positive electrostatic potentials on the surface. The blue area represents the most negative electrostatic potential, and the red represents the most positive electrostatic potential. The positive electrostatic potential on H_2 demonstrates its potential to donate a hydrogen bond, while the negative electrostatic potential on N_3 demonstrates its potential to accept a hydrogen bond. This indicates that the proton transfer takes place between the positive electrostatic H_2 atom and negative electrostatic N_3 atom.

Natural population analysis (NPA) and Hirshfeld charge are used to analysis the charge transfer quantificationally, and the results are shown in Table 3. The trend of NPA and Hirshfeld charges are the same. In three types of solvents, the Hirshfeld charges of N_3 are −0.143 (ACN), −0.144 (DCM), −0.146 (CH), and O_1 are −0.211 (ACN), −0.209 (DCM), −0.200 (CH), respectively, which shows that electronegativity of N_3 is enhanced and that of O_1 weakened with the polarity of the solvents decreasing. Therefore, as the solvent polarity decreasing, the attraction of N_3 to H_2 is improved, promoting the progress of ESIPT, which is the same with our above verdict.
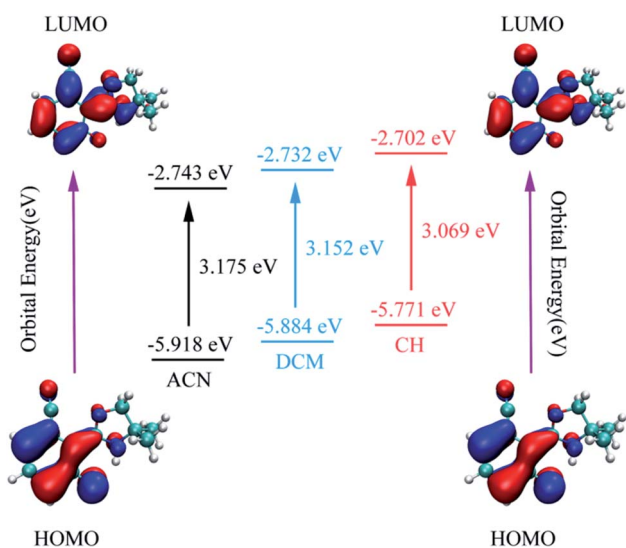

Fig. 5 The calculated frontier molecular orbitals (HOMO and LUMO) of NOHPO in the S_1 state and its transition energy.
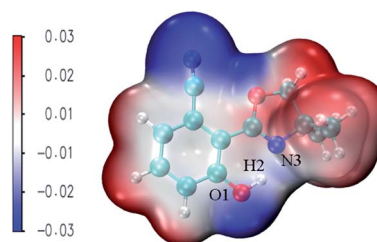

Fig. 6 The total electron density isosurfaces mapped with MEPS[48] for the NOHPO-enol form in ACN.

Table 3 Calculated charge NPA and Hirshfeld charge of O_1, H_2, N_3 atoms

	NPA charge						Hirshfeld charge					
	O_1		H_2		N_3		O_1		H_2		N_3	
	S_0	S_1	S_0	S_1	S_0	S_1	S_0	S_1	S_0	S_1	S_0	S_1
ACN	−0.653	−0.732	0.503	0.463	−0.528	−0.518	−0.211	−0.389	0.102	0.122	−0.143	−0.048
DCM	−0.651	−0.727	0.504	0.463	−0.528	−0.521	−0.209	−0.385	0.102	0.121	−0.144	−0.050
CH	−0.641	−0.710	0.504	0.463	−0.530	−0.530	−0.200	−0.369	0.104	0.119	−0.146	−0.057
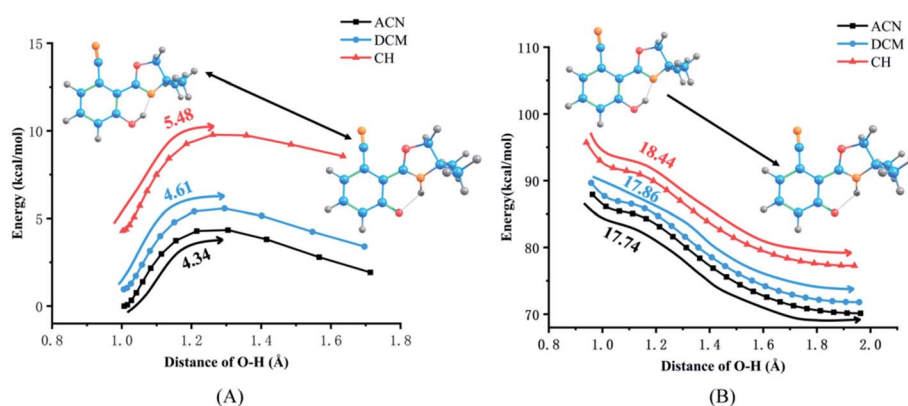
Fig. 7 Potential energy curves of the S_0 (A) and S_1 (B) states of NOHPO as a function of the O_1–H_2 bond length in ACN, DCM, CH.

Potential-energy curves

The PECs of NOHPO in the S_0 and S_1 states are established to unveil the effects of different solvents on the progress of ESIPT. PECs are shown in Fig. 7. The S_0 state has a lower relative energy than that in the S_1 state, indicating that NOHPO is unstable in the S_1 state. The reaction potential energy of ESIPT in the S_1 state is 17.74 kcal mol^{-1} in ACN, 17.86 kcal mol^{-1} in DCM, and 18.44 kcal mol^{-1} in CH, as shown in Fig. 7. With photoexcitation, H_2 can transfer to N_3 easily, so that the NOHPO molecule can transform from enol tautomer to keto tautomer. This also indicates that low-polar solvents facilitate the reaction of proton transfer. Proton transfer reaction barriers in the S_0 state are 4.34 kcal mol^{-1} (ACN), 4.61 kcal mol^{-1} (DCM), and 5.48 kcal mol^{-1} (CH), respectively. NOHPO molecules can be transformed from enol tautomer to keto tautomer due to the low reaction barrier of proton transfer. However, the unstable keto tautomer, whose energy is high, would return to a stable enol tautomer.

In summary, the progress of ESIPT can generalize that NOHPO molecules can be excited to the S_1 state upon photoexcitation. In the S_1 state, all NOHPO molecules transform to tautomeric structures *via* ESIPT, which when back to the S_0 state *via* radiation transition finally turn back to the normal structure spontaneously.

structure parameters and PECs imply that the hydrogen bond is greatly strengthened in the S_1 state, so that H_2 can transfer to N_3 easily, and the hydrogen bond in H_2–N_3 transforms into a covalent bond. The results of electronic spectra show that the maximum emission wavelength of the fluorescence spectrum has a bathochromic shift as the polarity decreases, so the range of emission wavelength can be regulated by solvents. In addition, the IR vibration spectrum, RDG analysis, charge distribution and PECs imply that ESIPT are favorable as the polarity decreases. Thus, the ESIPT of NOHPO in the different solvents is in the order of CH > DCM > ACN. The solvation effect is proved, and the relevance between the hydrogen bond and ESIPT in numerous solvents are also investigated.

Conflicts of interest

There are no conflicts to declare.

Acknowledgements

Conclusion

To sum up, the solvation effect and the ESIPT mechanism in three different solvents are illustrated by employing DFT and TD-DFT methods with the IEFPCM solvation model. Related

References

1 J. Zhao, H. Dong, H. Yang and Y. Zheng, *Org. Chem. Front.*, 2018, **5**, 2710–2718.
2 X. Luo, Y. Yang and Y. Li, *J. Mol. Liq.*, 2020, **319**, 114145.

3 W.-M. Kwok, C. Ma and D. L. Phillips, *J. Am. Chem. Soc.*, 2008, **130**, 5131–5139.

4 T. Schultz, E. Samoylova, W. Radloff, I. V. Hertel, A. L. Sobolewski and W. Domcke, *Science*, 2004, **306**, 1765–1768.

5 M. Rini, *Science*, 2003, **301**, 349–352.

6 D. Sicinska, D. G. Truhlar and P. Paneth, *J. Am. Chem. Soc.*, 2001, **123**, 7683–7686.

7 Y. Qi, Z. Tang, H. Zhan, Y. Wang, Y. Zhao, X. Fei, J. Tian, L. Yu and J. Liu, *Spectrochim. Acta Mol. Biomol. Spectrosc.*, 2020, **224**, 117359.

8 Z. Tang, Y. Qi, Y. Wang, P. Zhou, J. Tian and X. Fei, *J. Phys. Chem. B*, 2018, **122**, 3988–3995.

9 W. Xu, S. Liu, H. Sun, X. Zhao, Q. Zhao, S. Sun, S. Cheng, T. Ma, L. Zhou and W. Huang, *J. Mater. Chem.*, 2011, **21**, 7572.

10 G.-J. Zhao and K.-L. Han, *Acc. Chem. Res.*, 2012, **45**, 404–413.

11 G.-J. Zhao, R.-K. Chen, M.-T. Sun, J.-Y. Liu, G.-Y. Li, Y.-L. Gao, K.-L. Han, X.-C. Yang and L. Sun, *Chem. –Eur. J.*, 2008, **14**, 6935–6947.

12 G.-J. Zhao, J.-Y. Liu, L.-C. Zhou and K.-L. Han, *J. Phys. Chem. B*, 2007, **111**, 8940–8945.

13 Z. Tang, Y. Wang, D. Bao, M. Lv, Y. Yang, J. Tian and L. Dong, *J. Phys. Chem. A*, 2017, **121**, 8807–8814.

14 Z. Tang, Y. Yang, Y. Yang, Y. Wang, J. Tian and X. Fei, *J. Lumin.*, 2018, **194**, 785–790.

15 P. Zhou and K. Han, *Acc. Chem. Res.*, 2018, **51**, 1681–1690.

16 X. Li, Y. Guo and D. Yang, *Theor. Chem. Acc.*, 2020, **139**, 181.

17 Y. Yang, W. Shi, Y. Chen, F. Ma and Y. Li, *J. Lumin.*, 2021, **229**, 117698.

18 L. Jia and Y. Liu, *Spectrochim. Acta Mol. Biomol. Spectrosc.*, 2020, **242**, 118719.

19 A. Shahraki, A. Ebrahimi, S. Rezazadeh and R. Behazin, *Mol. Syst. Des. Eng.*, 2021, **6**, 66–79.

20 G. Zhao, Y. Yang, C. Zhang, Y. Song and Y. Li, *J. Lumin.*, 2021, **230**, 117741.

21 C.-C. Hsieh, P.-T. Chou, C.-W. Shih, W.-T. Chuang, M.-W. Chung, J. Lee and T. Joo, *J. Am. Chem. Soc.*, 2011, **133**, 2932–2943.

22 T. Chatterjee, M. Mandal, A. Das, K. Bhattacharyya, A. Datta and P. K. Mandal, *J. Phys. Chem. B*, 2016, **120**, 3503–3510.

23 G. Cui, Z. Lan and W. Thiel, *J. Am. Chem. Soc.*, 2012, **134**, 1662–1672.

24 Y.-H. Hsu, Y.-A. Chen, H.-W. Tseng, Z. Zhang, J.-Y. Shen, W.-T. Chuang, T.-C. Lin, C.-S. Lee, W.-Y. Hung, B.-C. Hong, S.-H. Liu and P.-T. Chou, *J. Am. Chem. Soc.*, 2014, **136**, 11805–11812.

25 S. Janakipriya, S. Tamilmani and S. Thennarasu, *RSC Adv.*, 2016, **6**, 71496–71500.

26 S. Liu, M. Qin, Q. Lu, L. Lin, C.-K. Wang, J. Fan and Y. Song, *Spectrochim. Acta Mol. Biomol. Spectrosc.*, 2021, **254**, 119685.

27 O. Alici and D. Aydin, *J. Photochem. Photobiol. Chem.*, 2021, **404**, 112876.

28 Y. Cheng, S. Wang, J. Zhang, J. Cao and Y. Qu, *J. Mol. Struct.*, 2020, **1221**, 128824.

29 G. Kumar, I. Singh, R. Goel, K. Paul and V. Luxami, *Spectrochim. Acta Mol. Biomol. Spectrosc.*, 2021, **247**, 119112.

30 S. Paul and P. Banerjee, *Sens. Actuators, B*, 2021, **329**, 129172.

31 R. Kaushik, R. Sakla, N. Kumar, A. Ghosh, V. D. Ghule and D. A. Jose, *Sens. Actuators, B*, 2021, **328**, 129026.

32 K. Anusuyadevi, S. P. Wu and S. Velmathi, *J. Photochem. Photobiol. Chem.*, 2020, **403**, 112875.

33 P. Zhang, Y. Xiao, Q. Zhang, Z. Zhang, H. Yu and C. Ding, *New J. Chem.*, 2019, **43**, 7620–7627.

34 S. Benson, A. Fernandez, N. D. Barth, F. de Moliner, M. H. Horrocks, C. S. Herrington, J. L. Abad, A. Delgado, L. Kelly, Z. Chang, Y. Feng, M. Nishiura, Y. Hori, K. Kikuchi and M. Vendrell, *Angew. Chem., Int. Ed.*, 2019, **58**, 6911–6915.

35 D. Gobel, D. Duvinage, T. Stauch and B. J. Nachtsheim, *J. Mater. Chem. C*, 2020, 14.

36 M. J. Frisch, G. W. Trucks, H. B. Schlegel, G. E. Scuseria, M. A. Robb, J. R. Cheeseman, G. Scalmani, V. Barone, G. A. Petersson, H. Nakatsuji, X. Li, M. Caricato, A. V. Marenich, J. Bloino, B. G. Janesko, R. Gomperts, B. Mennucci, H. P. Hratchian, J. V. Ortiz, A. F. Izmaylov, J. L. Sonnenberg, D. Williams-Young, F. Ding, F. Lipparini, F. Egidi, J. Goings, B. Peng, A. Petrone, T. Henderson, D. Ranasinghe, V. G. Zakrzewski, J. Gao, N. Rega, G. Zheng, W. Liang, M. Hada, M. Ehara, K. Toyota, R. Fukuda, J. Hasegawa, M. Ishida, T. Nakajima, Y. Honda, O. Kitao, H. Nakai, T. Vreven, K. Throssell, J. A. Montgomery Jr., J. E. Peralta, F. Ogliaro, M. J. Bearpark, J. J. Heyd, E. N. Brothers, K. N. Kudin, V. N. Staroverov, T. A. Keith, R. Kobayashi, J. Normand, K. Raghavachari, A. P. Rendell, J. C. Burant, S. S. Iyengar, J. Tomasi, M. Cossi, J. M. Millam, M. Klene, C. Adamo, R. Cammi, J. W. Ochterski, R. L. Martin, K. Morokuma, O. Farkas, J. B. Foresman and D. J. Fox, *Gaussian 16, Revision C.01*, Wallingford CT, 2016.

37 C. Lee, W. Yang and R. G. Parr, *Phys. Rev. B: Condens. Matter Mater. Phys.*, 1988, **37**, 785–789.

38 B. Miehlich, A. Savin, H. Stoll and H. Preuss, *Chem. Phys. Lett.*, 1989, **157**, 200–206.

39 E. Cancès, B. Mennucci and J. Tomasi, *J. Chem. Phys.*, 1997, **107**, 3032–3041.

40 S. Miertuš, E. Scrocco and J. Tomasi, *Chem. Phys.*, 1981, **55**, 117–129.

41 B. Mennucci, E. Cancès and J. Tomasi, *J. Phys. Chem. B*, 1997, **101**, 10506–10517.

42 R. Cammi and J. Tomasi, *J. Comput. Chem.*, 1995, **16**, 1449–1458.

43 A. Schäfer, C. Huber and R. Ahlrichs, *J. Chem. Phys.*, 1994, **100**, 5829–5835.

44 A. Schäfer, H. Horn and R. Ahlrichs, *J. Chem. Phys.*, 1992, **97**, 2571–2577.

45 E. R. Johnson, S. Keinan, P. Mori-Sánchez, J. Contreras-García, A. J. Cohen and W. Yang, *J. Am. Chem. Soc.*, 2010, **132**, 6498–6506.

46 T. Lu and F. Chen, *J. Comput. Chem.*, 2012, **33**, 580–592.

47 W. Humphrey, A. Dalke and K. Schulten, *J. Mol. Graph.*, 1996, **14**, 33–38.

48 T. Lu and F. Chen, *J. Mol. Graph. Model.*, 2012, **38**, 314–323.